



HAL
open science

Frame-based reflectance estimation from multispectral images for weed identification in varying illumination conditions

Anis Amziane, Olivier Losson, Benjamin Mathon, Aurelien Dumenil, Ludovic Macaire

► To cite this version:

Anis Amziane, Olivier Losson, Benjamin Mathon, Aurelien Dumenil, Ludovic Macaire. Frame-based reflectance estimation from multispectral images for weed identification in varying illumination conditions. Tenth International Conference on Image Processing Theory, Tools and Applications (IPTA 2020), IEEE, Nov 2020, Paris, France. 10.1109/IPTA50016.2020.9286692 . hal-02994446

HAL Id: hal-02994446

<https://hal.science/hal-02994446>

Submitted on 19 Jan 2023

HAL is a multi-disciplinary open access archive for the deposit and dissemination of scientific research documents, whether they are published or not. The documents may come from teaching and research institutions in France or abroad, or from public or private research centers.

L'archive ouverte pluridisciplinaire **HAL**, est destinée au dépôt et à la diffusion de documents scientifiques de niveau recherche, publiés ou non, émanant des établissements d'enseignement et de recherche français ou étrangers, des laboratoires publics ou privés.

Frame-based reflectance estimation from multispectral images for weed identification in varying illumination conditions

Anis Amziane*, Olivier Losson*, Benjamin Mathon*, Aurélien Dumenil†, Ludovic Macaire*

* Univ. Lille, CNRS, Centrale Lille, UMR 9189 – CRISTAL –

Centre de Recherche en Informatique Signal et Automatique de Lille, F-59000 Lille, France

email: {anis.amziane, olivier.losson, benjamin.mathon, ludovic.macaire}@univ-lille.fr

† Chambre d’Agriculture de la Somme, F-80090 Amiens, France

email: a.dumenil@somme.chambagri.fr

Abstract—To prevent the growth of weeds in precision farming, multispectral imaging has gained much interest for its ability to provide vegetation images with a high spectral resolution. However, spectral reflectance computation is an issue when the image is assembled from successive frames acquired under varying illumination conditions. In this study, we present a method to estimate reflectance from images acquired by a linescan camera in such conditions. Because rows in a given channel are associated to different illumination conditions, we process the image row-wise to improve reflectance estimation. Experimental segmentation results show that our method is a good candidate to effectively identify crops from weeds.

Index Terms—Multispectral imaging, Reflectance estimation, Illumination, Precision farming, Weed detection, Linescan camera.

I. INTRODUCTION

In most cases, removal of the weeds in agricultural fields involves the application of abundant quantities of chemical herbicides, which is harmful to the environment regardless of their success in increasing crop productivity. To optimize the application of herbicides in crop fields, precision spraying can be considered thanks to recent advances in imaging sensors. The sensors originally used in agricultural fields are either monochromatic or color-based ones [1]. A critical limitation is that they use average spectral information over wide wavelength ranges, resulting in a lack of detailed information in specific narrow bands. During the last decade, more sophisticated multispectral sensors have been manufactured and deployed in crop fields leading to precision farming applications like pest and disease detection [2], plant classification [3], and weed detection [4]–[6].

Multispectral cameras collect spectral data over a wide spectral range and provide the ability to investigate spectral responses of soils and vegetated surfaces in narrow spectral bands. Two categories of devices can be distinguished in multispectral image acquisition [7]. “Snapshot” (multi-sensor or filter array-based) devices build the image from a single shot. Although

this technology provides multispectral images at video frame rate, the few acquired channels may not be sufficient to fully explore the vegetation spectral signatures. “Multishot” (tunable filter or illumination-based, push-broom, spatio-spectral linescan) devices build the image from several and successive frame acquisitions. Although restricted to still scenes, they provide images with a high spectral resolution. In this study, we use a multishot camera to acquire outdoor multispectral radiance images of plant parcels in a greenhouse. From this radiance information, the spectral reflectance is estimated as an illumination-invariant spectral signature of each species.

Several methods have been proposed to compute reflectance thanks to prior knowledge about cameras or illumination conditions [8]–[10]. In field conditions, typical methods first estimate the illumination by including a reference device (a white diffuser or a ColorChecker Chart) in the scene [5], [11]–[13]. Then, the reflectance is estimated at each pixel p by channel-wise dividing the value of the radiance image at p by the pixel values characterizing the white diffuser or the ColorChecker white patch. In [14], an extension to the multispectral domain of four algorithms traditionally applied to RGB images is proposed to estimate the illumination. In [15], a bragg-grating-based multispectral camera is used to acquire outdoor radiance images. Two white diffusers are used for reflectance computation, one is included at the bottom image border and the other is fully visible. In [16], illumination variation is compensated in outdoor condition using a subspace model proposed in [17], and enhanced by learning a historical database of illumination and reflectance spectra along various natural lighting conditions. A multispectral camera is used in conjunction with a skyward pointing spectrometer in [18] to estimate reflectance from the acquired scene radiance.

These methods require specific devices and knowledge about the spectral sensitivity functions (SSFs) of the sensor filters, and may include a learning step. They also often assume constant incident illumination during the successive frame acquisitions (scans). In outdoor conditions however, the illumination may vary significantly across scans that last several seconds (e.g., 12s with our camera for an integration time of 1.5ms

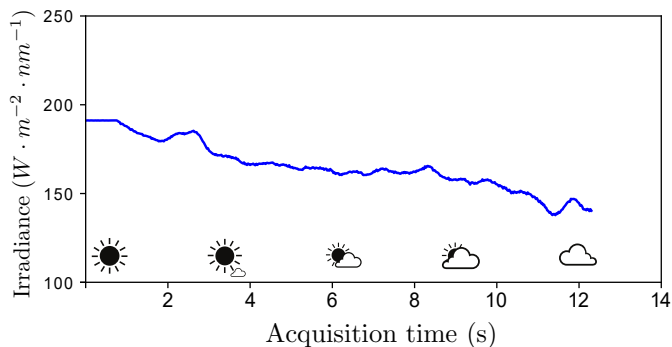


Fig. 1: Illumination variation at wavelength 500nm during an acquisition of an outdoor multispectral image.

that is suited to most outdoor conditions). Fig. 1 illustrates this phenomenon by showing the variation of the incident irradiance at wavelength 500nm during one of our outdoor frame acquisitions, measured by the *AvaSpec-ULS2048L* spectrometer. In this paper, we propose a learning-free reflectance estimation method that is robust to illumination variations during the acquisition of frames used to provide multispectral images.

The paper is organized as follows. In Sec. II, we give details about the multispectral image acquisition process in outdoor conditions using a linescan camera. In Sec. III, we propose a method for scene reflectance estimation from a multispectral radiance image acquired in uncontrolled and varying illumination conditions. Sec. IV presents an experimental evaluation of the proposed method, and weed/crop segmentation results using the estimated reflectance. Finally, conclusions are drawn in Sec. V.

II. MULTISPECTRAL IMAGE ACQUISITION

A. Image formation model

We consider a multispectral camera that embeds a sensor covered with spectrally sensitive filters and provides a multispectral radiance image $\mathbf{I} = \{I^k\}_{k=1}^K$ with K spectral channels thanks to the acquisition of frames. Assuming homogeneous spectral sensitivity of the sensor, the value I_p^k of channel I^k at pixel p can be expressed as:

$$I_p^k = Q \left(\tau \cdot \int_{\Omega} E(\lambda) \cdot R_p(\lambda) \cdot T^k(\lambda) \cdot o_p(\lambda) d\lambda \right), \quad (1)$$

where τ is the frame integration time, Ω is the working spectral domain, $E(\lambda) \in [0, 1]$ is the relative spectral power distribution of the illumination which is assumed to homogeneously illuminate all surface elements of the scene, $R_p(\lambda) \in [0, 1]$ is the spectral reflectance at wavelength λ of the surface element s observed by pixel p , $o_p(\lambda) \in [0, 1]$ is the optical attenuation of the lens for pixel p at λ . The radiance $E(\lambda) \cdot R_p(\lambda) \cdot o_p(\lambda)$ is filtered according to the SSF $T^k(\lambda)$ of the filter k associated to a narrow spectral band. The value I_p^k is given by the quantization of the received energy on B bits by the function Q .

B. Snapscan camera

The Snapscan [19] is a multispectral camera manufactured by IMEC that embeds a single matrix sensor, covered by a series of narrow stripes of Fabry-Perot integrated filters. It provides $K = 141$ spectral channels whose central wavelengths range from $\lambda^1 = 475.1\text{nm}$ to $\lambda^{141} = 901.7\text{nm}$ with a variable center step (from 0.5nm to 5nm). Specifically, each filter is associated to 5 adjacent rows of 2048 pixels, and samples a band from the visible (VIS) or near infrared (NIR) spectral domain according to its SSF $T^k(\lambda)$ with a full width at half maximum between 2nm and 10nm.

During acquisitions, both the object and camera remain static. The sensor moves linearly from bottom to top behind the lens inside the Snapscan with a spatial step of 5 pixel rows, and records a two-dimensional *frame* f_i at each time t_i , $i = 1 \dots N$. A frame f_i is spatially organized as juxtaposed stripes of 5 consecutive pixel rows. Each stripe f_i^k , $k = 1 \dots K$, contains the spectral information of the scene radiance filtered according to the SSF $T^k(\lambda)$ of the filter k centered at wavelength λ^k .

The multispectral image should then be assembled from N successively acquired frames $\{f_i\}_{i=1}^N$ (see Fig. 2). All the stripes associated to filter k in all the acquired frames are stacked to provide an assembly $\{f_i^k\}_{i=1}^N$. The scene part common to all the assemblies is considered to form the spectral channels. Finally, the Snapscan delivers a multispectral radiance image $\mathbf{I} = \{I^k\}_{k=1}^K$ composed of $K = 141$ channels quantized on $B = 10$ bits.

Note that before the frame acquisitions, the Snapscan uses its internal shutter to acquire a dark frame f_{dark} whose values are subtracted pixel-wise from the acquired frames. Therefore, the pixel value expressed by (1) is assumed to be free from thermal noise.

III. REFLECTANCE ESTIMATION

A. Reflectance computation

To compute reflectance according to the linear image formation model of (1), the following assumptions need to be verified:

- (i) The illumination is spatially uniform and does not vary during the successive acquisition of the frames.
- (ii) Each of the Fabry-Perot filters has an ideal SSF:

$$T^k(\lambda) = \delta(\lambda - \lambda^k) = \begin{cases} 1 & \text{if } \lambda = \lambda^k, \\ 0 & \text{otherwise.} \end{cases} \quad (2)$$

- (iii) Each SSF of the Fabry-Perot filters is angle-independent, thus vignetting effect only depends on pixel location.

The discrete version of (1) can be expressed as:

$$I_p^k = \tau \cdot \sum_{l=1}^K E(\lambda^l) \cdot R_p(\lambda^l) \cdot T^k(\lambda^l) \cdot o_p(\lambda^l). \quad (3)$$

Note that the quantization function Q is omitted here since the different terms are already considered as quantized.

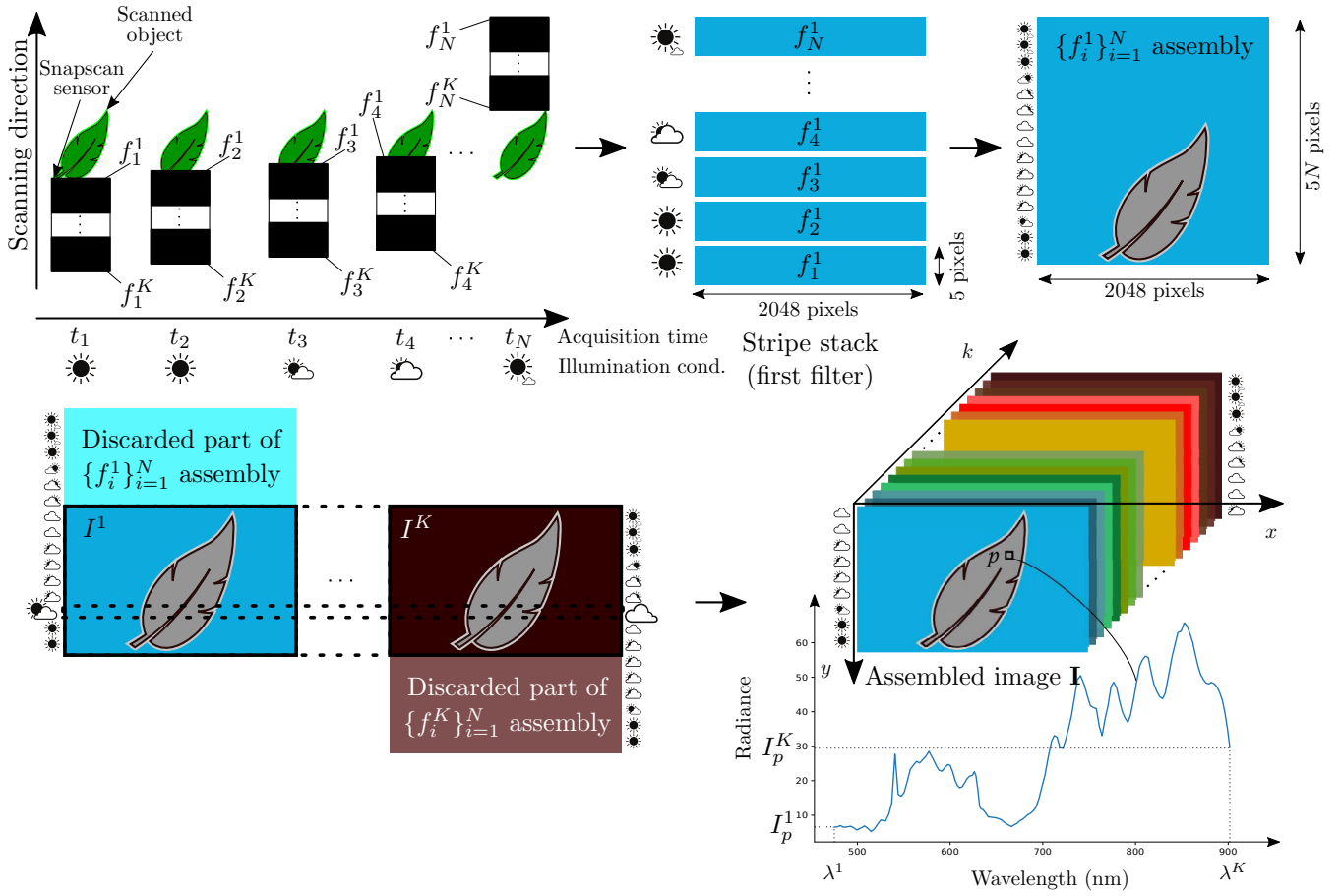


Fig. 2: Frame acquisition and assembly in varying illumination conditions (top) and K -channel multispectral image (bottom).

Assumption (ii) is not verified in practice: there is no multispectral camera with such a fine resolving power. However, to the extent of our knowledge, the filters embedded in the Snapscan are very narrow and approximate this assumption to the best at present. We can then write:

$$I_p^k = \tau \cdot E(\lambda^k) \cdot R_p(\lambda^k) \cdot o_p(\lambda^k). \quad (4)$$

The reflectance of a surface element s observed by pixel p for the spectral band centered at λ^k is then expressed as:

$$R_p(\lambda^k) = \frac{I_p^k}{\tau \cdot E(\lambda^k) \cdot o_p(\lambda^k)}. \quad (5)$$

B. Reflectance estimation under constant illumination

The term $E(\lambda^k) \cdot o_p(\lambda^k)$ in (5) characterizes the illumination in the sensor domain for channel k , and can be experimentally estimated by acquiring a full-field image \mathbf{I}_{wd} of a white diffuser. This calibration tile is supposed to reflect the incident light for all $\lambda \in \Omega$ with a constant diffuse reflection factor ρ_{wd} ($\rho_{\text{wd}} = 95\%$ for our Sphere Optics Spectralon[®]). Using the same image formation model and assumptions as for \mathbf{I} (see (4)), each value of \mathbf{I}_{wd} is then expressed as:

$$I_{\text{wd},p}^k = \tau_{\text{wd}} \cdot E(\lambda^k) \cdot \rho_{\text{wd}} \cdot o_p(\lambda^k), \quad (6)$$

where τ_{wd} is the frame integration time used to acquire \mathbf{I}_{wd} . Plugging (6) into (5) then yields the estimated reflectance \hat{R}_p^k for channel k at pixel p :

$$\hat{R}_p(\lambda^k) \stackrel{\text{def}}{=} \hat{R}_p^k = \rho_{\text{wd}} \cdot \frac{I_p^k}{I_{\text{wd},p}^k} \cdot \frac{\tau_{\text{wd}}}{\tau}. \quad (7)$$

Note that this reflectance estimation method implicitly compensates the vignetting effect. Since the white diffuser and the object occupy the same (full) field of view, I_p^k and $I_{\text{wd},p}^k$ are affected by the same optical attenuation whose effect vanishes after division. We consider the reflectance estimated by this method as a reference and denote it as $\hat{\mathbf{R}}_{\text{ref}}$.

C. Reflectance estimation under varying illumination

The Snapscan assembles a multispectral radiance image from individual frames acquired at different successive times. Due to illumination variations during frame acquisitions in outdoor (see Fig. 1), the illumination conditions associated to the values of the assembled radiance image vary both across pixel rows for a given channel and across channels for a given row (see Fig. 2). To estimate the reflectance, we then need to estimate the illumination condition for each channel and each row.

Inspired by [15], [16], we propose to mount a white diffuser

on the acquisition device so that the sensor vertically observes a portion of it at the right border of each frame. Once the N frames have been assembled as an image, an area W of width 250 pixels represents the white diffuser (see Fig. 3). Each row of this area is used to estimate the specific illumination condition under which the scene part associated to the same pixel row has been acquired.

Because reflectance cannot be estimated according to (7) any longer, the vignetting effect cannot be compensated as in Sec. III-A. To accurately estimate the reflectance, we need to spatially correct the vignetting effect on each channel of the radiance image \mathbf{I} .

1) *Vignetting correction*: To compute a correction factor for each pixel, we use a look-up table (LUT) approach [20] because it requires no knowledge about the optical device behavior. To generate LUT correction factors, one first acquires a full-field image \mathbf{I}_{wd} of a white diffuser under a spatially uniform and constant illumination, and in a dark room to avoid ambient light influence. The vignetting effect in the object radiance image \mathbf{I} is then corrected pixel-wise and channel-wise to provide the corrected image $\tilde{\mathbf{I}}$ as:

$$\tilde{I}_p^k = \frac{I_{\text{wd}}^k}{I_{\text{wd},p}^k} \cdot I_p^k. \quad (8)$$

The first term is the correction factor. It implies I_{wd}^k , namely the median value of m pixels with the highest values over I_{wd}^k to discard saturated or defective pixel values.

2) *Row-wise (rw) based reflectance estimation*: Since pixels in each row of $\tilde{\mathbf{I}}$ are associated to the same illumination condition according to the spatial uniformity assumption, we estimate the reflectance from the radiance image $\tilde{\mathbf{I}}$ in a row-wise manner (see Fig. 3). Moreover, the attenuation is spatially uniform (and equal to a constant α^k for all p associated to channel index k) after vignetting correction. The reflectance at pixel p associated to channel index k is then deduced from (5) as:

$$R_p(\lambda^k) = \frac{\tilde{I}_p^k}{\tau \cdot E_{y(p)}(\lambda^k) \cdot \alpha^k}. \quad (9)$$

For a given row $y(p)$, the illumination $E_{y(p)}(\lambda^k)$ is the same at any pixel p . We estimate it from the median value $\tilde{I}_{W,y(p)}^k$ of the m highest pixel values of the white diffuser (W) in this row. This median value satisfies (6), which provides the rw-based estimated reflectance as:

$$\hat{R}_{\text{rw},p}^k = \rho_{\text{wd}} \cdot \frac{\tilde{I}_p^k}{\tilde{I}_{W,y(p)}^k}. \quad (10)$$

IV. EVALUATION OF REFLECTANCE ESTIMATION

A. Overview

An image acquisition campaign was conducted in a greenhouse under skylight by the Chambre d'Agriculture de la Somme in early April 2019. The targeted plants are beet, wheat, bean, and barley for crops, and datura, thistle, goose-foot, foxtail, and barnyard grass for weeds. For our exper-

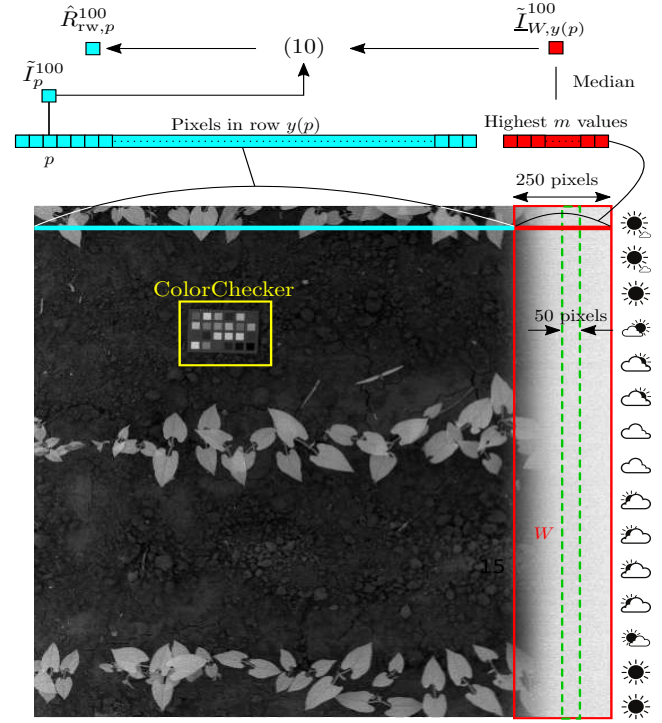


Fig. 3: rw-based reflectance estimation ($k = 100$, $\lambda^{100} = 780\text{nm}$).

iments we use a database composed of $M = 63$ radiance images acquired on different days and at different times of the day, each of which represents a single plant species and incorporates a GretagMacbeth™ ColorChecker Chart.

We compare the quality of the rw method (setting $m = 11$) with the results obtained by two methods that are generally dedicated to images acquired with snapshot or linescan cameras in controlled illumination conditions. The classical white-average (wa) method uses the surface of a white diffuser included in the scene to estimate the illumination for each channel. We adopt the wa implementation by considering a subset W_s of W in our images (see dashed green rectangle in Fig. 3). The max-spectral (ms) method provides good performance when estimating the illumination in multispectral images with various band combinations [14]. It uses the maximum pixel value within each channel. The reflectance is estimated at each pixel in each channel by wa and ms methods as:

$$\hat{R}_{\text{wa},p}^k = \rho_{\text{wd}} \cdot \frac{\tilde{I}_p^k}{\frac{1}{|W_s|} \sum_{p \in W_s} \tilde{I}_p^k}, \quad (11)$$

and:

$$\hat{R}_{\text{ms},p}^k = \frac{\tilde{I}_p^k}{\max_{p \in X} \tilde{I}_p^k}, \quad (12)$$

where $|W_s|$ is the number of white diffuser pixels considered for wa implementation, and X is the set of vegetation and soil pixels (i.e., all image pixels but W and those of the

ColorChecker).

B. Reflectance estimation error

To evaluate the accuracy of reflectance estimation, we use the patches of the ColorChecker (see Fig. 3). Let $\hat{\mathbf{R}}_*$, $*$ \in {rw, wa, ms}, denote the reflectance image estimated by either of the three tested methods (see (10)–(12)).

All surface elements of a patch are assumed to have the same spectral response. Each patch P_j , $j = 1 \dots 24$, is then represented by a K -dimensional reflectance vector $\hat{\mathbf{R}}_{*,P_j}$ whose k^{th} component is computed as the average value in channel k over all the pixels characterizing the patch. This vector is compared to the reference reflectance $\hat{\mathbf{R}}_{\text{ref},P_j}$ of the same patch estimated according to (7) from an image of the ColorChecker acquired in laboratory under controlled illumination conditions. Note that the ColorChecker is placed at various spatial coordinates in the images of our database. In case of high vegetation density, it is placed on the top of a wooden block to prevent patch occlusions by leaves. Thus we use a 15×15 pixel window around the automatically detected center of each patch to ensure all these pixels belong to the same patch whatever the image.

We objectively asses each estimated reflectance image thanks to the mean absolute error (MAE) and the angular error $\Delta\theta$ of each patch P_j , given by:

$$\text{MAE}(\hat{\mathbf{R}}_{\text{ref},P_j}, \hat{\mathbf{R}}_{*,P_j}) = \frac{1}{K} \sum_{k=1}^K |\hat{R}_{\text{ref},P_j}^k - \hat{R}_{*,P_j}^k|, \quad (13)$$

and:

$$\Delta\theta(\hat{\mathbf{R}}_{\text{ref},P_j}, \hat{\mathbf{R}}_{*,P_j}) = \arccos \left(\frac{\langle \hat{\mathbf{R}}_{\text{ref},P_j}, \hat{\mathbf{R}}_{*,P_j} \rangle}{\|\hat{\mathbf{R}}_{\text{ref},P_j}\|_2 \cdot \|\hat{\mathbf{R}}_{*,P_j}\|_2} \right), \quad (14)$$

where $\langle \cdot, \cdot \rangle$ is the dot vector product, and $\|\cdot\|_2$ is the Euclidean norm. When $\Delta\theta$ of two vectors (spectra in our case) is equal to zero, it means that these two vectors are collinear. We compute the average mean absolute error $\overline{\text{MAE}}_*$ and angular error $\overline{\Delta\theta}_*$ over all patches of all estimated reflectance images. We also compute the average channel-wise mean absolute error $\overline{\text{MAE}}_*^k$ over all patches of all reflectance images.

Tab. I shows the average mean absolute and angular errors over all images in the database for the three tested methods. We can see that in terms of quality of reflectance estimation, the rw-based method provides the lowest average mean absolute and angular errors.

Considering the channel-wise error (see Fig. 4), the highest error rates in the range [475nm, 750nm] (VIS domain) are obtained by ms because it only analyzes pixels of background and vegetation that strongly absorb the incident light. Hence, illumination estimation is biased using ms in this domain. In the range [750nm, 901nm] (NIR domain), the light reflection factor of vegetation is high (it appears brighter in Fig. 3), and the ms method gives very similar results as rw. The wa method gives acceptable results along the working domain [475nm, 901nm] of the Snapscan camera, while our rw method provides the lowest error rates.

TABLE I: REFLECTANCE ESTIMATION ERRORS

Method *	$\overline{\text{MAE}}_*(\%)$	$\overline{\Delta\theta}_*$ (rad)
rw	7.479	0.092
wa	10.188	0.094
ms	20.636	0.354

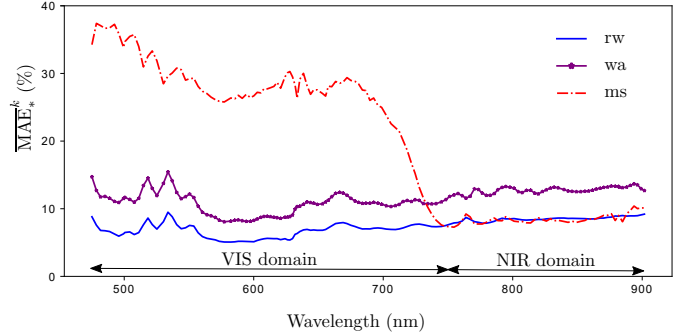


Fig. 4: Channel-wise MAE of reflectance estimation.

C. Multispectral image segmentation

We now briefly evaluate the contribution of the rw-based reflectance estimation method for segmentation tasks. To assess the robustness of rw against illumination variations, we consider an extra outdoor radiance image of a crop (beet) and weed (thistle) species (see Fig. 5), acquired on a different day than those present in our database. Vegetation pixels are separated from the background using the NDVI index [21]. A pixel p is considered as a vegetation pixel if its NVDI index is greater than a manual threshold \mathcal{T} , namely:

$$\frac{\hat{R}_{\text{rw},p}^{140} - \hat{R}_{\text{rw},p}^{68}}{\hat{R}_{\text{rw},p}^{140} + \hat{R}_{\text{rw},p}^{68}} \geq \mathcal{T}, \quad (15)$$

where $\lambda^{68} = 678.2\text{nm}$ and $\lambda^{140} = 899.2\text{nm}$ with the Snapscan. \mathcal{T} is set to 0.45 in our case. Note that a vegetation pixel in any rw-based reflectance image is also considered as such in its corresponding radiance image and reflectance images estimated by wa and ms.

The vegetation pixels are manually annotated by an expert in agronomy that builds the segmentation ground truth as two classes. Our radiance database contains 13 beet images and 10 thistle images with different growth stages. From each image we randomly extract 2000 pixels, each being characterized by a feature vector of reflectance (or radiance) values of dimension $K = 141$. To reduce residual noise and within-class variability, the reflectance/radiance is averaged channel-wise over a 5×5 pixel window around each pixel. To analyze equiprobable classes, the pixel sets are balanced against the lowest class size (see Tab. II).

The segmentation process obeys a supervised scheme. All pixels in the balanced set are used as learning samples. We use the non-parametric 5-nearest neighbors classifier and the Euclidean distance measure.

Tab. III shows the classification accuracies. The rw method

TABLE II: NUMBER OF PIXELS PER CLASS

Class	Extracted pixels	Balanced set	Test pixels
Beet	26,000	20,000	674,131
Thistle	20,000	20,000	340,866
Total	46,000	40,000	1,014,997

TABLE III: CLASSIFICATION ACCURACIES

Spectral signature	radiance	rw	wa	ms
Accuracy (%)	76.86	88.93	77.83	62.91

provides the highest classification accuracy, which suggests that rw-based reflectance is the most robust against illumination variations. Fig. 5 show the segmentation results obtained on the input multispectral image rendered as RGB in Fig. 5(a) using the CIE Standard Illuminant D65 with the CIE 1931 2° Standard Observer. Segmentation using radiance spectra (see Fig. 5(c)) leads to thistle over-detection whereas wa- and ms-based reflectance spectra (see Figs. 5(e) and 5(f)) lead to thistle under-detection. rw-based spectra (see Fig. 5(d)) provide a good discrimination between the two classes.

V. CONCLUSION

This paper proposes a method to estimate spectral reflectance from multispectral radiance images acquired in outdoor illumination conditions. We show that classical methods of reflectance estimation are not adapted in these conditions for multishot devices such as the Snapscan. Indeed, the illumination that varies during the frame acquisitions affects the reflectance estimation quality. Therefore, we propose to estimate the illumination at a frame level following the proposed row-wise (rw) approach. As an application of the rw-based reflectance, an image segmentation by pixel classification is performed. As a future work, the segmentation process will be extended to more images with complex scenes. Furthermore, the most suited spectral bands for this task should be identified and used to specify a multispectral camera that is less sensitive to outdoor illumination variation.

ACKNOWLEDGEMENT

This work was supported by the Région Hauts-de-France, the Chambre d'Agriculture de la Somme, and the ANR-11-EQPX-23 IrDIVE platform.

REFERENCES

- [1] D. J. Mulla, "Twenty five years of remote sensing in precision agriculture: Key advances and remaining knowledge gaps," *Biosystems Engineering*, vol. 114, pp. 358–371, Apr. 2013.
- [2] A.-K. Mahlein, "Detection, identification, and quantification of fungal diseases of sugar beet leaves using imaging and non-imaging hyperspectral techniques," Ph.D. dissertation, Universität Bonn, Nov. 2010.
- [3] S. Haug, A. Michaels, P. Biber, and J. Ostermann, "Plant classification system for crop /weed discrimination without segmentation," in *IEEE Winter Conference on Applications of Computer Vision*, Mar. 2014, pp. 1142–1149.
- [4] A. Wendel and J. Underwood, "Self-supervised weed detection in vegetable crops using ground based hyperspectral imaging," in *2016 IEEE International Conference on Robotics and Automation (ICRA)*, May 2016, pp. 5128–5135.

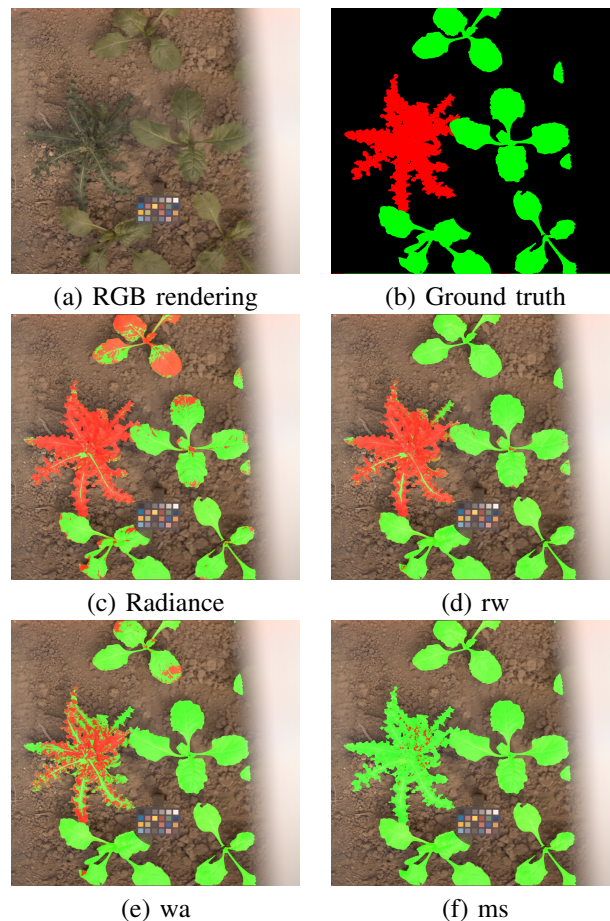


Fig. 5: Vegetation segmentation results. Beet is shown as green and thistle as red.

- [5] F. Feyaerts and L. van Gool, "Multi-spectral vision system for weed detection," *Pattern Recognition Letters*, vol. 22, no. 6, pp. 667–674, 2001.
- [6] F. Lin, D. Zhang, Y. Huang, X. Wang, and X. Chen, "Detection of corn and weed species by the combination of spectral, shape and textural features," *Sustainability*, vol. 9, no. 8, 2017.
- [7] N. Hagen and M. W. Kudenov, "Review of snapshot spectral imaging technologies," *Optical Engineering*, vol. 52, no. 9, p. 090901, Sep. 2013.
- [8] H.-L. Shen, P.-Q. Cai, S.-J. Shao, and J. H. Xin, "Reflectance reconstruction for multispectral imaging by adaptive Wiener estimation," *Optics Express*, vol. 15, no. 23, pp. 15 545–15 554, Nov. 2007.
- [9] H. A. Khan, J.-B. Thomas, J. Y. Hardeberg, and O. Laligant, "Multi-spectral camera as spatio-spectrophotometer under uncontrolled illumination," *Optics Express*, vol. 27, no. 2, pp. 1051–1070, Jan. 2019.
- [10] V. Heikkinen, R. Lenz, T. Jetsu, J. Parkkinen, , M. Hauta-Kasari, and T. Jääskeläinen, "Evaluation and unification of some methods for estimating reflectance spectra from RGB images," *Journal of the Optical Society of America A*, vol. 25, no. 10, pp. 2444–2458, Nov. 2008.
- [11] M.-A. Bourgeon, J.-N. Paoli, G. Jones, S. Villette, and C. Gée, "Field radiometric calibration of a multispectral on-the-go sensor dedicated to the characterization of vineyard foliage," *Computers and Electronics in Agriculture*, vol. 123, pp. 184–194, 2016.
- [12] S. Del Pozo, P. Rodríguez-González, D. Hernández-López, and B. Felipe-García, "Vicarious radiometric calibration of multispectral camera on board unmanned aerial system," *Remote Sensing*, vol. 6, pp. 1918–1937, Feb. 2014.
- [13] K. Uto, H. Seki, G. Saito, and Y. Kosugi, "Characterization of rice paddies by a UAV-mounted miniature hyperspectral sensor system," *IEEE J-STARS*, vol. 6, no. 2, pp. 851–860, Apr. 2013.
- [14] H. A. Khan, J.-B. Thomas, J. Y. Hardeberg, and O. Laligant, "Illuminant

- estimation in multispectral imaging,” *Journal of the Optical Society of America A*, vol. 34, no. 7, pp. 1085–1098, Jul. 2017.
- [15] J. Eckhard, T. Eckhard, E. M. Valero, J. L. Nieves, and E. G. Contreras, “Outdoor scene reflectance measurements using a bragg-grating-based hyperspectral imager,” *Applied Optics*, vol. 54, no. 13, pp. D15–D24, May 2015.
- [16] W. Alexander and U. James, “Illumination compensation in ground based hyperspectral imaging,” *ISPRS Journal of Photogrammetry and Remote Sensing*, vol. 129, pp. 162–178, Jul. 2017.
- [17] D. Mark and F. Graham, “Analytic solution for separating spectra into illumination and surface reflectance components,” *Journal of the Optical Society of America. A, Optics, image science, and vision*, vol. 24, pp. 294–303, Mar. 2007.
- [18] Z. Chuiqing, K. Douglas, R. Murray, and S. Bo, “Fusion of multispectral imagery and spectrometer data in UAV remote sensing,” *Remote Sensing*, vol. 9, p. 696, Jul. 2017.
- [19] J. Pichette, W. Charle, and A. Lambrechts, “Fast and compact internal scanning CMOS-based hyperspectral camera: the Snapscan,” in *Proceedings of the SPIE Electronic Imaging Annual Symposium: Photonic Instrumentation Engineering IV*, vol. 10110, San Francisco, CA, USA, 2017, pp. 1–10.
- [20] W. Yu, “Practical anti-vignetting methods for digital cameras,” *IEEE Trans. Consum. Electron.*, vol. 50, no. 4, pp. 975–983, 2004.
- [21] P. S. Thenkabail, R. B. Smith, and E. De Pauw, “Evaluation of narrowband and broadband vegetation indices for determining optimal hyperspectral wavebands for agricultural crop characterization,” *Photogrammetric Engineering & Remote Sensing*, vol. 68, no. 6, pp. 607–621, Jun. 2002.